

Lateral Nanoconcentrator Nanowire Multijunction Photovoltaic Cells

Investigators

Professors:

H.-S. Philip Wong (Department of Electrical Engineering)
Peter Peumans (Department of Electrical Engineering)
Mark Brongersma (Department of Materials Science)
Yoshio Nishi (Department of Electrical Engineering)

Graduate researchers:

Ying Chen, Jason Parker, Trudie Wang

Post-doctoral researchers:

Xinyu Bao, Aaron Hryciw

Senior Research Associate:

Jim McVittie

Abstract

During the project period, we developed a straightforward and physically intuitive procedure to optimize the net overall absorption of a thin-film solar cell using periodic metal nanostructures. We investigated the plasmon-enabled absorption enhancements due to the aforementioned effects by performing full-field electromagnetic simulations based on the finite-difference frequency-domain (FDFD) method.

In order to investigate the capabilities of metal nanoantennas to enhance absorption in the nanowires, the ring resonator antenna was selected to represent the geometry that would be responsible for spectral splitting and electromagnetic field concentration. Using FDTD simulations, we shown that the ring antenna geometry is both effective at spectral splitting and optical field concentration, and hence a prime candidate for a lateral multijunction cell.

We developed a low-cost non-lithographic method to fabricated nanoring antennas that can be extended for large scale applications. We also successfully demonstrated the nanowire growth inside the nanorings facilitated by the advantages of above method.

We grew III-V nanowires and investigated their photoelectrochemical applications (PEC) for hydrogen generation. We demonstrated a GaP nanowire PV for PEC applications in which a p-n junction is not required.

The III-V-N MOCVD has been set up at Stanford University for high efficiency solar cell study.

We succeeded in synthesis of anatase TiO₂ nanoframe directly on conductive and transparent substrates using templated Sol-Gel deposition. The new concept of “nanoframe” is introduced to make nanowire structure more robust, which greatly increases the mechanical stability of nanowire array solar cell. We demonstrated the feasibility of a multi-layer nanoframe scheme to extend the thickness of TiO₂ nanostructure.

Introduction

The objective of this research project is to develop a novel type of multijunction photovoltaic cell that uses lateral arrays of semiconductor nanowires (NWs) of various bandgaps as the elements that convert optical energy into electrical energy. In contrast to conventional stacking multijunction cells, the NWs of varying bandgap will not be connected in series in our approach. Instead, a specially-designed nanostructured metal film is used to split the incident broadband solar spectrum and localize spectral energy in different lateral spatial locations (spectral splitting and concentration) coinciding with the location of the NWs of the optimized bandgap. The same nanostructured metal film also allows for current extraction from each nanowire separately such that photocurrent matching is not required. This allows us to use a wide range of bandgaps (depending on the performance of the lateral metal spectral splitter and concentrator) without requiring current matching. It also allows broader choices on materials which can approach the ideal performance limits due to the less spectral mismatch losses. This removes the most important efficiency bottleneck of multijunction cells such that efficiencies $>45\%$ may be achieved over a wide range of spectral conditions. The NWs can be grown by the vapor-liquid-solid (VLS) method and the sol-gel approach, both of which have the potential for low cost manufacturing since epitaxial growth conditions are easily met at moderate temperatures over the short length scale of a NW. To demonstrate the lateral multijunction principle, we will use NWs of materials that span the solar spectrum, including Si, Ge, III-V materials and other abundant, non-toxic, low-cost elements, e.g., TiO_2 .

Results

I. Electromagnetic Simulations of the Lateral Concentrator

1. Metal Strips

We developed a straightforward and physically intuitive procedure to optimize the net overall absorption of a thin-film solar cell using periodic metal nanostructures [1]. It was demonstrated that one can simultaneously take advantage of 1) the high near-fields surrounding the nanostructures close to their surface plasmon resonance frequency and 2) the effective coupling to waveguide modes supported by the semiconductor film through an optimization of the array properties. We use a simple model system consisting of a periodic array of Ag strips on a silica-coated, thin Si film supported by a silica substrate (See Figure 1) to illustrate these concepts.

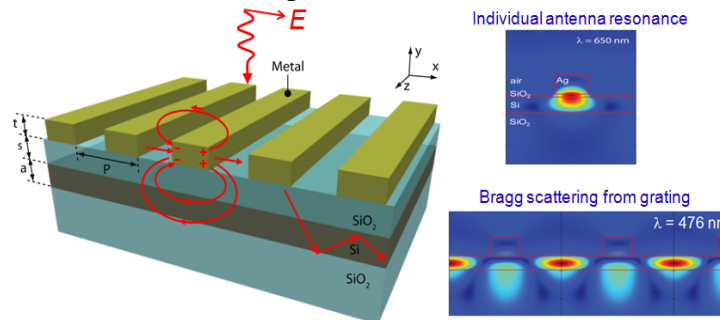


Figure 1: (Left) Schematic of our rapid prototyping platform with a periodic metal grating. It illustrates how absorption can be enhanced via light concentration near the surface plasmon resonance frequency of the metal stripes and by Bragg scattering normally incident light into a waveguided mode. (Right) Full-field simulations of the different absorption enhancement mechanisms.

The metal strip geometry was chosen because of its simple cross-sectional shape, which is described by just two parameters (thickness and width). These strips serve as plasmonic resonator antennas and are capable of very effectively light concentration at frequencies near their surface plasmon resonance. This resonance frequency critically depends on the strip geometry and its dielectric environment [2] It is well-established that deep subwavelength particles cause relatively strong absorption and less scattering as compared to larger particles. No significant benefits from light scattering and trapping can thus be expected from very small strips. Our studies provided beneficial effects on the short circuit current for strips with characteristic sizes in the range from 50 nm – 100 nm. Substantially larger strips behave like optical mirrors, reflecting most of the incident radiation back into free space. In contrast to near-field concentration effects, the lateral spacing of the strips governs the excitation of waveguide modes. The number of allowed waveguide modes and their dispersion is determined by the thickness of the Si layer and this important parameter should be chosen carefully. Optimum coupling results were found when the reciprocal lattice vector of the Ag strip-array (grating) is matched to the k-vector of a waveguide mode supported by the Si slab. We have also started working on aperiodic gratings that naturally have more spatial frequencies and can enhance light absorption at more wavelengths than the periodic gratings. The SiO₂ layers we used can offer high optical transparency and can provide excellent electrical surface passivation of the Si. The top oxide also serves as a spacer layer between the metal and the absorbing Si layer whose thickness can be controlled with extreme precision using thermal oxidation. From our studies, we found that putting metallic particles in direct contact with an absorbing semiconductor material induces an undesired, strong damping of the surface plasmon resonance that is responsible for the enhanced light absorption. Spacing of a few tens of nanometer between the particles and the semiconductor were found to be ideal for a number of different cell designs.

We investigated the plasmon-enabled absorption enhancements due to the aforementioned effects by performing full-field electromagnetic simulations based on the finite-difference frequency-domain (FDFD) method [3]. FDFD simulations enable the use of tabulated materials parameters and adaptive grid spacing. For the periodic arrays under study, we implemented periodic boundary conditions and perfectly matched layer (PML) boundary conditions were used at the top and bottom of the simulation volume. We calculated the absorption in the Si slab for a normally incident plane wave using $\omega \cdot \text{Im}(\epsilon) \int_V |E|^2 dV'$, where E is the local, simulated electric field and V is the volume of the Si slab. The absorption enhancements at various wavelengths, $I(\lambda)$, were then determined from the ratio of the absorbed light in the Si slab with and without metal strips.

By generating absorption enhancement maps vs. photon energy and reciprocal lattice vector, it has become straightforward to separate out contributions from near-field light concentration by localized surface plasmon resonances and enhanced light trapping by coupling to waveguide modes; these features tend to show up in different locations in such maps and exhibit different dispersion properties. By investigating trends in these physical quantities with the relevant cell design parameters, intuition for optimizing the

cell can be rapidly acquired. We have looked in detail at the specific example of an array of Ag strips on a thin (50 nm) Si film cell and enhancements in photocurrent of over 43% could be obtained. Even higher enhancements ($> 50\%$) could be reached for thicker cells (100nm-10 μm) for which more waveguide modes can contribute to the overall enhancement. Although we have only considered the benefit of this strategy on the enhancement in the short circuit current, beneficial effects on the open circuit voltage are to be expected as well due to the enhanced photo carrier injection levels, similar to concentrator cells. This general design strategy is currently extended to 3-dimensional arrays and aperiodic structures that exhibit even higher efficiencies.

2. Metallic Nanorings

In order to investigate the capabilities of metal nanoantennas to enhance absorption in the nanowires, the ring resonator antenna was also selected to perform the spectral splitting and electromagnetic field concentration. Despite its wide, rounded geometry, an important characteristic of the ring resonator is that it still maintains the ability to focus the electric field along the ring and nanowire axis such that it is locally and uniformly enhanced within the ring cavity when ring resonance occurs [4-10]. Although surface plasmon (SP) resonances are characteristic of many subwavelength nanostructures, the ring geometry is unique in that it has the ability to concentrate the electric field of a SP mode into a smaller volume while still retaining the ability to redshift the plasmon resonance peak without the material losses, retardation effects and radiation damping associated with larger nanodimers[11, 12]. Additionally, the ring structure has the advantage of being inherently polarization independent because of its rotational symmetry.

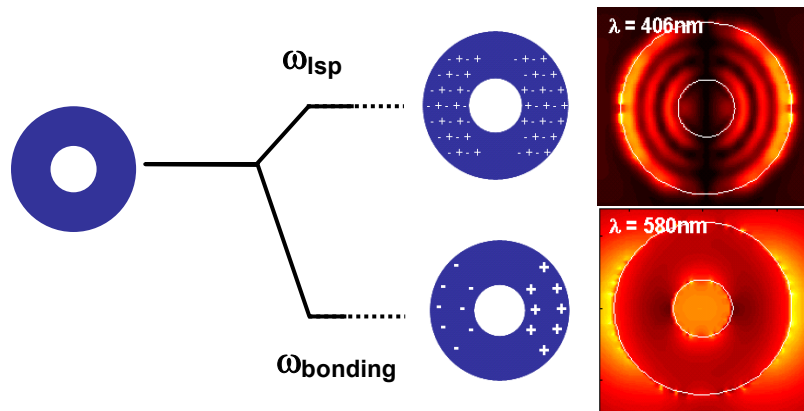


Figure 2: Energy-level diagram for SP resonance of metal nanorings in the visible region where the resonance wavelengths correspond to a ring thickness of 40nm, inner diameter of 40nm and a height of 100nm. The lower energy mode results from the symmetric bonding mode of the ring and focuses the energy inside the cavity of the ring by exciting a strong dipolar resonance that involves the entire ring perimeter. The higher energy mode results from the LSP mode near the material resonance of the metallic nanoantenna and concentrates mostly on the external surface of the ring.

A localized surface plasmon (LSP) mode, which occurs on the external surface of the ring, and a so-called symmetric bonding mode pave the way for the construction of a lateral multijunction PV cell with the junctions formed using nanowires of different bandgaps. Figure 2 shows how the electromagnetic energy in the LSP mode of an Ag ring is concentrated primarily along the external surfaces of the ring and how the symmetric

bonding mode contains the field energy within the cavity of the ring. The aim is to ensure that the nanowires absorb only at parts of the solar spectrum they are ideal for. The next section describes how the LSP and symmetric bonding mode can be used to separate different parts of the solar spectrum into different spatial regions.

To determine how effectively electromagnetic energy can be concentrated and absorbed by the semiconductor nanowires, 3-dimensional finite difference time domain (FDTD) analysis has been used to simulate lateral concentrators exposed to frequencies of light ranging across the visible and near infra-red (NIR) spectrum. Lumerical, a commercial FDTD software package, has a built in parallel solver and has successfully been used to model plasmonic effects in various complex geometries and match them to experimental results [13-15].

The geometry we simulated consisted of an Ag ring resonator with a nanowire positioned inside the ring and a similar nanowire placed in the gap between rings as shown in Figure 3. The simulation was carried out initially using perfectly matched layers (PML) for the boundary conditions in both the x- and y-directions. In this geometry, a plane wave propagates into the xy-plane along the z-axis and is polarized along the x-direction. The nanowires and ring antenna are both kept to a constant height of 100nm and deposited on a SiO₂ substrate in an air environment. The motivation behind the placement of the nanowires both inside and just outside the ring was to locate them in regions of maximum field enhancement to maximize the amount of energy absorbed by the semiconductor material at plasmonic resonance.

In order to demonstrate how spectral and spatial separation and enhancement can increase absorption in both nanowires, two different materials were selected to represent the internal and external nanowires in the geometry. GaAs was placed inside the ring since it is inherently a good direct bandgap absorber with a bandgap of 1.43eV in the NIR range, where it can benefit from the electromagnetic field enhancement within the cavity. Outside the ring, AlAs was used for the nanowire since its relatively higher bandgap energy of 2.16eV will benefit from the LSP resonance. Placing a nanowire just outside the ring also introduces asymmetry into the geometry and allows for better coupling into the LSP mode.

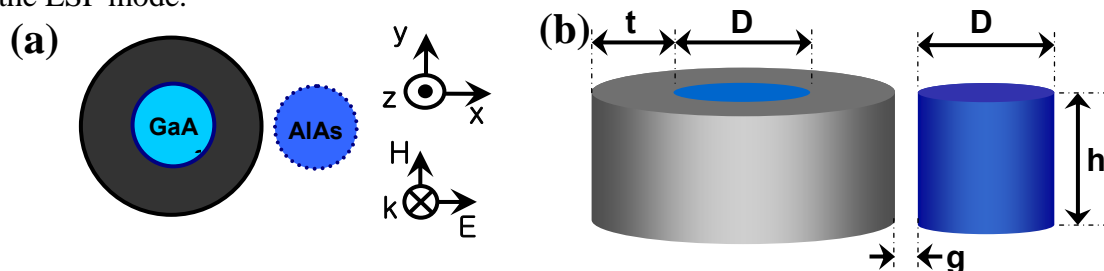


Figure 3: (a) Ring and nanowire geometry modeled using FDTD. The boundary conditions in all direction use a perfectly matched layer (PML) for the single geometry case. For the periodic array, a periodic boundary condition was used in the x- and y- direction while PML was retained for the z-direction. The nanowire inside the ring (light blue) is GaAs while the external nanowire (dark blue) is AlAs. The ring antenna is modeled as Ag. (b) FDTD geometry shown in 3-dimensions where d is the diameter of both nanowires and the inner diameter of the ring antenna, t is the ring thickness, h is the height of the nanowires and the ring, and g is the gap size between the ring and the external nanowire. In our geometry, the plasmon resonance is most sensitive to the t - d ratio.

Ag was selected to represent the ring nanoantenna due to its high density of free electrons which resonate in the visible regime when the ring diameter is subwavelength. Although Au has similar properties, it is considerably lossier due to low-energy interband transitions. Ag has interband transitions that begin at energy of about 3.8eV—about 1.3 eV higher than that of Au—and hence is more suitable for plasmon mode excitation [10, 11, 16].

The results of the simulations of the structure from Figure 3 with the GaAs nanowire inside the ring and the AlAs nanowire outside the ring are as follows. Absorption enhancement is plotted as a function of wavelength for the GaAs and AlAs nanowire in Figure 4a. The plot shows evidence of enhanced absorption in different spectral regions, indicating that absorption can be both spectrally selective and localized spatially. In the case of the AlAs nanowire, there is a 6x enhancement at resonance near where the LSP mode of the individual ring occurs. The GaAs nanowire shows a much stronger enhancement of about 380x at around where the ring's symmetric bonding mode occurs. Figure 4b and c show the electric field magnitude $|E|$ profiles across the $z = 50\text{nm}$ plane midway through the nanowires and ring antenna at the symmetric bonding and LSP resonance modes, respectively. These field profiles show a large absorption peak at $\lambda = 780\text{nm}$ (Figure 4b), a strong dipolar field enhancement outside the ring with minimal penetration into the metal, and a weak interaction of the higher energy LSP mode with the incident plane wave (Figure 4c). The LSP excited on the surface creates a dipolar field at around $\lambda = 460\text{nm}$, where resonance occurs, and induces a dipole in the external nanowire. This leads to strong field enhancement between the LSP and the external nanowire, which funnels the electromagnetic energy into the AlAs nanowire and results in an increase in absorption.

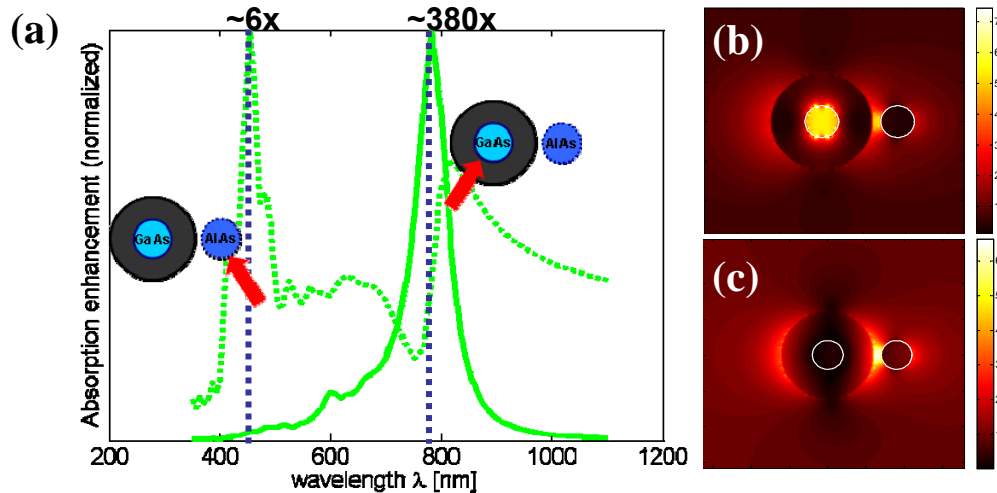


Figure 4: (a) Normalized absorption enhancement plotted as a function of wavelength for an Ag ring antenna 40nm thick using PML boundary conditions to represent a single geometry. Absorption enhancement is defined as the amount of power absorbed in the nanowire with a ring present divided by the power absorbed in the nanowire when there is no ring present. The dotted line represents absorption enhancement in the external AlAs nanowire while the solid line represents the absorption in the internal GaAs nanowire. Both are normalized to fit on the same axis but the actual magnitude of the enhancement differs sharply and is noted above the plot. (b-c) Electric field magnitude $|E|$ plotted for the symmetric bonding and LSP mode at 780nm and 460nm respectively where the resonance peaks lie in the spectral response. The results are for a geometry with $D = 40\text{nm}$ and $h = 100\text{nm}$.

The two main parameters that were further explored in our geometry were the nanowire diameter and the ring antenna thickness. In agreement with literature [4, 5, 17-20], the location of the plasmon resonance peaks and level of field enhancement was found to be most sensitive to the ratio between the ring thickness and diameter. As this ratio is decreased by making the ring thinner or the diameter larger, coupling between the inner and outer walls grows stronger so that the symmetric bonding mode becomes increasingly red-shifted. Figure 5a and b show the spectral responses of the GaAs and AlAs nanowire, respectively, that result from changing the thickness-to-diameter ratio of the ring geometry. The inner diameter is kept constant at 40nm while increasing the outer radius such that the ring thickness increases from 0nm to 50nm.

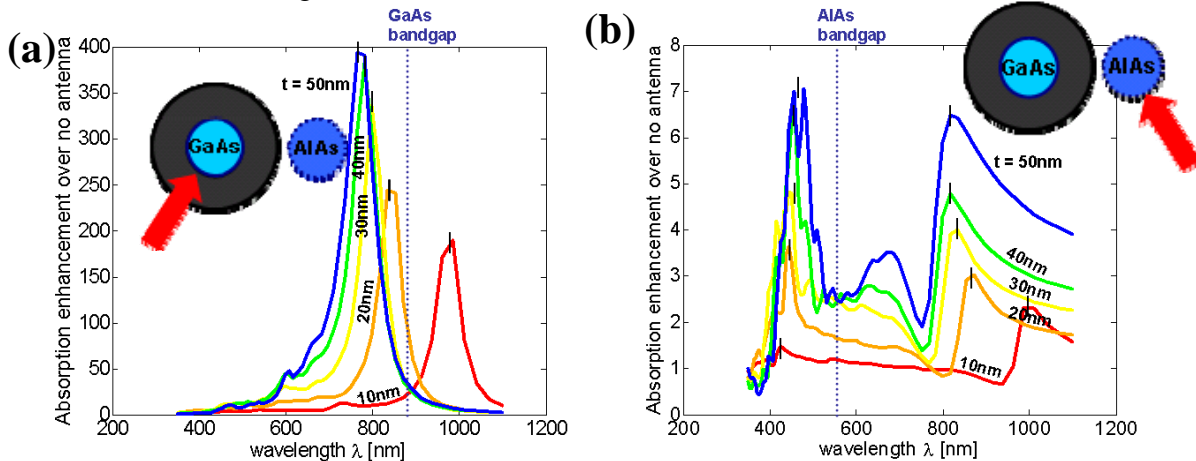


Figure 5: (a) Absorption enhancement in the internal GaAs nanowire plotted as a function of wavelength for various thicknesses of the Ag ring antenna ranging from 0 to 50nm for a single geometry. (b) Absorption enhancement in the external AlAs nanowire plotted for the same geometries. In all cases, the results are for a geometry with $D = 40\text{nm}$ and $h = 100\text{nm}$. As both plots show, a decreasing thickness leads to a redshift in the peaks due to the symmetric bonding mode. This shift occurs with increasing sensitivity as the ring gets thinner and mode coupling and splitting increases. Decreased enhancement is observed for both the LSP and symmetric bonding mode as confinement increases.

In addition to a redshift in the symmetric bonding resonance of the ring in the NIR regime, the decrease in the thickness to diameter ratio also results in a reduced level of enhancement along with an increase in the linewidth of both the bonding and LSP resonance peaks. These trends illustrate the tradeoff between a thicker and thinner ring. In the latter case, there is more mode splitting and tunability due to an increased mode coupling, but the field enhancement is no longer as large or homogeneous over the entire cavity or ring surface since the increased confinement of the plasmon current results in more material loss in the antenna itself.

The most promising feature of the geometry we have simulated is the ability to tune the strong dipolar bonding resonance and hence the absorption enhancement peak very near the wavelength regions of the solar spectrum where a large part of the photon energy lies and where the band edge of materials would ideally lie to avoid thermalization losses, but where many of the same materials are inherently weak absorbers because of the proximity to the band edge. This improvement in light absorption will help to increase photocurrent and hence improve cell performance [21].

II. Nanoring Antenna Fabrication

Lithography is a conventional technique to fabricate nanoantennas and a second step of lithography is required to grow nanowires on specific locations with high alignment accuracy to place the catalysts. We developed a low cost and simple method to fabricate metal nanoring with a single Au nanoparticle (NP) in the center for nanowire growth. The fabrication process is shown in figure #. Ag rings with 200 nm outer diameter were fabricated around Au NPs on chips of Si (111). First, the Si was cleaned followed by coating Au colloids with diameter ~200 nm. Ag ~100 nm was then sputtered conformally on the samples. The Ag was etched using a directed Ar etch which removed the Ag exposed while the Ag shadowed by Au sphere was reserved. Ag etches approximately twice as fast as Au under the given Ar sputtering conditions. SEM micrograph (Figure 6, upper right) indicates that the Ag on top of the Au NPs and in bare areas of the substrate were removed, leaving Ag rings around gold spheres. Once the Au NP was exposed, germanium nanowires were grown using a two-step temperature profile (Figure 6, lower right). Samples were heated to 380°C for 3 minutes to initiate nanowire growth and the temperature was lowered to 300°C for continued growth with minimal sidewall deposition.

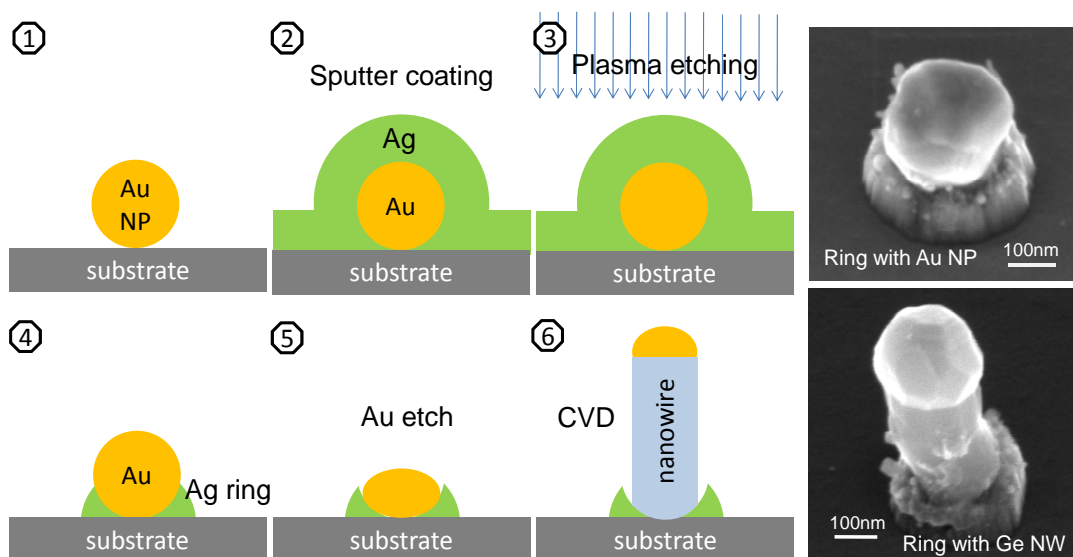


Figure 6: (Left) Fabrication process of nanoring antennas with Au nanoparticles (NP) as catalysts in the center for nanowires growth. (Upper right) Fabricated nanoring with a Au NP in the center. 45° tilted SEM. (Lower right) Ge nanowires grown using Au NP catalyst surrounded by nanoring antenna. 45° tilted SEM.

This process uses one step deposition and etching to fabricate both nanoring antennas and catalyst NPs for nanowires growth at the same time. The nanowires will not grow from the Ag rings since the eutectic temperature between Ag and Ge is 651 °C which is much higher than that of Au and Ge at 360 °C. According to the nanoring dimension, nanowires with suitable bandgap energy can be grown to reach the optimal energy conversion. A schematic of the PV device is shown in Figure 7. Au catalysts will be removed after nanowires growth. The device fabrication is currently undergoing.

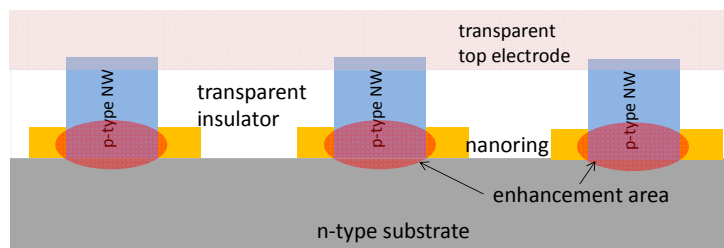


Figure 7: Schematic of the nanowires PV device with nanoring antennas.

IV. III-V NWs for Photoelectrochemical Applications and MOCVD Setting Up

Core-shell nanowire is an ideal structure for nanowire PVs, where a junction is formed in the radial direction between the core nanowire and shell material to extract the carriers [22]. The currently reported core-shell nanowire PVs are of much lower efficiency than the planar PVs due to challenges in making high quality core-shell structures. The primary challenge is doping.

We looked into alternative structures where no p-n junctions are required. When a semiconductor is immersed in a liquid, a junction is formed at the semiconductor-liquid interface [23]. Charge flows across that junction due to a potential difference between the two sides until electronic equilibrium is reached; this process causes the semiconductor bands to bend at the interface, forming a space charge region on the semiconductor side of the interface. Due to the electric field within this space charge region, photo-excited electrons and holes in this area of the semiconductor are easily separated, facilitating their extraction. Figure 8(a) illustrates a photoelectrochemical (PEC) example of a p-type thin film semiconductor in an aqueous electrolyte. In the nanowire case as shown in Figure 8 (b), a radial space-charge region is formed as the liquid surrounds the semiconductor. Due to the small diameter of the nanowire, the space charge region is formed throughout a large portion of the nanowire. Most of the photogenerated carriers will be excited within the space charge region, facilitating high efficient separation and extraction.

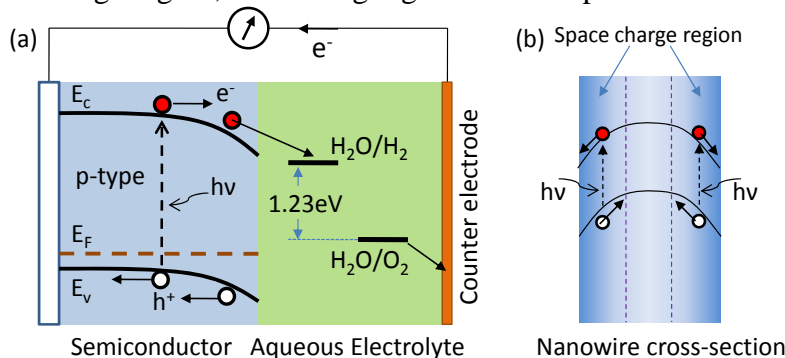


Figure 8: (a) A schematic of PEC cell using p-type semiconductor. Hydrogen evolution happens at the semiconductor-liquid interface, oxygen oxidation happens at the liquid-counter electrode interface. (b) Band bending and space charge region formation of a p-type semiconductor nanowire when immersed into aqueous electrolyte.

We investigated monolithic GaP nanowire PV for PEC hydrogen generation. GaP nanowires were grown on n-type Si (111) substrates using metal-organic chemical vapor deposition (MOCVD) with trimethylgallium (TMGa) and tertbutylphosphine (TBP)

precursors and Au nanoparticles as catalysts. The morphology and crystal structure characterization of the GaP nanowires are shown in *Figure 9*. The as grown GaP nanowires were slightly n-type. After growth, Zn based spin-on-dopant was used to dope the nanowires to p-type.

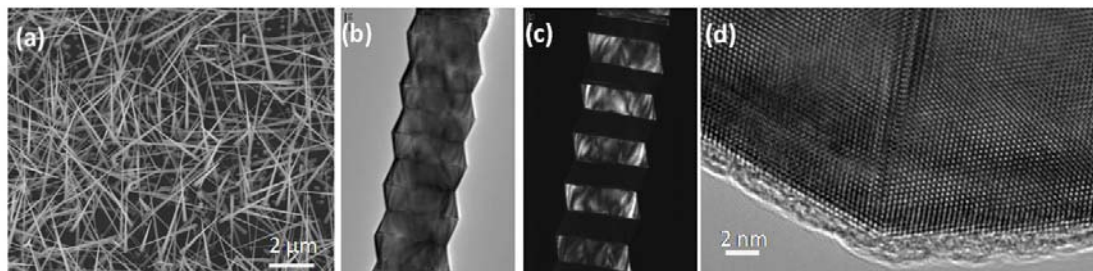


Figure 9: (a) SEM top view of the GaP nanowires on Si substrate. TEM structural characterization: (b) bright field, (c) dark field, and (d) high resolution TEM of the twinning.

Assessment of the photoactivity of undoped and doped GaP nanowires on the Si substrate was carried out. The photoelectrochemical testing was done in 0.1M H₂SO₄ in a 3-electrode cell with the supported nanowires as the working electrode, a Pt mesh counter electrode and a Ag/AgCl in saturated KCl reference electrode. Electrical contact to the silicon support was made by abrading the back surface and applying copper tape. The illumination source was a 1000W Xe lamp with AM1.5 filter and a potentiostat was used for data collection. Cyclic voltammetry under chopped illumination (1 Hz) revealed both p-type (cathodic) and n-type (anodic) photoactivity and a representative sweep for each material is shown in *Figure 10*. No significant photocurrent was observed for either the undoped bare Si or doped bare Si substrate (doped under the same conditions as the GaP nanowires). Doped GaP nanowires exhibited larger p-type photocurrent than the undoped nanowires. Dark and illuminated open circuit potential measurements, useful for determining the flat band potential and calculating the material band structure, were collected for undoped and doped GaP nanowires as well as the bare substrates. Initial calculations of the band edges for the doped GaP, based on the electrochemically determined flat band potential, reveal that it is thermodynamically possible to reduce protons to hydrogen in the entire range where cathodic photocurrent was observed. This evidence strongly supports that GaP nanowires are a photocathode of interest for the water-splitting reaction.

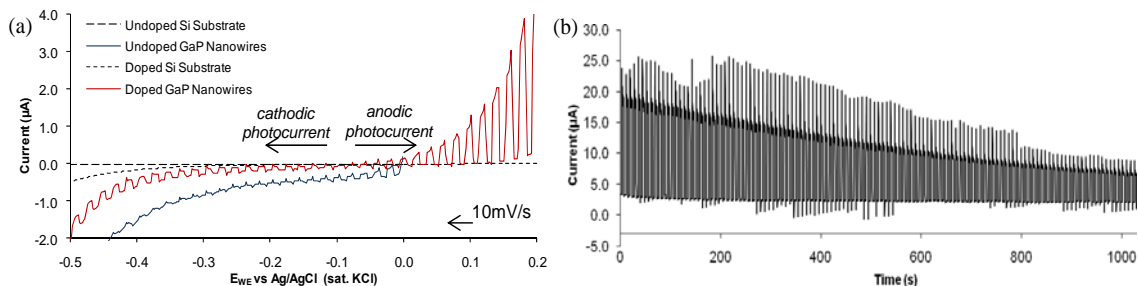


Figure 10: (a) Cyclic voltammogram showing photoactivity of doped GaP nanowires on a Si substrate. (b) Chronoamperometry at $E_{WE} = 0.4V$ vs. Ag/AgCl (sat. KCl) for doped GaP nanowires showing decaying anodic photocurrent.

The III-V-N MOCVD has been completed at Stanford University. The advantage of this MOCVD is the nitrogen source which can provide nitrogen doping for more flexible bandgap and lattice constant tuning as well as performance improvement such as stability.

V. Titanium Dioxide NW Dye-Sensitized Solar-Cells

1. TiO_2 Sol-Gel Growth and TiO_2 Etching

As mentioned in previous annual report, oxygen plasma was used to etch a transfer layer of polymer masked by a layer of self-assembled di-block copolymer. Further experiment results showed that after oxygen plasma etching, the polymer templates need to be treated with diluted hydrofluoric acid (HF) to remove the residue of the di-block copolymer mask which contains mainly of organosilicates. The organosilicate residue tends to induce non-electrical sol-gel deposition, which blocks the openings of the pores before the electrical sol-gel process fills up the pores in the template and results in voids in the nanopillars (Figure 11(a)). When the residue of organosilicate is removed, pores remained open before being filled with titanyl hydroxide gel before the forming of the top layer (Figure 11(b)).

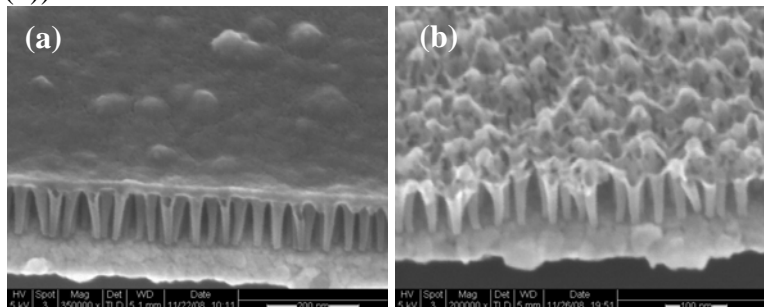
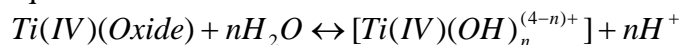


Figure 11. 45° SEM cross-sectional pictures of titania nanopillars sol-gel deposited in 200 nm PMGI templates on platinum coated silicon substrates, with the working electrode potential of $-1.147V$ versus $Ag/AgCl$ reference (a) for 30sec without the hydrofluoric treatment, and (b) for 30sec with a diluted hydrofluoric (50:1) of 15sec before the electrodeposition.

We found that wet etching after sol-gel or stir-bar agitation during the sol-gel process can effectively and selectively remove the top layer. Though CF_4 plasma etching is a commonly used method to remove oxide, wet etching is more favorable due to simplicity. In [24] and [25], the authors used 4 M sulfuric acid to dissolve the titanyl hydroxide gel. Our experimental results suggested that sulfuric acid with concentration between 0.25 M and 1 M can partially remove the freshly deposited gel by controlling the soaking time. But once the gel is left in room temperature for more than a day, even 4 M sulfuric acid failed to dissolve the dried titanyl hydroxide gel. Also, we found that the sulfuric acid etching of gel in a wet state resulted in fairly non-uniform etching across a $1cm^2$ sized sample, so we looked into other chemistries that might etch the titanyl hydroxide gel. Titania solid dissolves under the presence of H_2O_2 yielding some hydrated complexes as represented in the equation:



We tried to use 30wt% peroxide H_2O_2 , mixed with 29wt% ammonia hydroxide NH_4OH in volumn ratio of 1:1, to etch dried titanyl hydroxide gel. NH_4OH was added to neutralize H^+ and push the reaction to the right, favoring the dissolution of Ti (IV) oxide.

As a result, this solution can etch both the room temperature dried and the 110 °C overnight dried titanyl gels. *Figure 12* shows resulted titania morphologies before (a, c) and after (b, d) the removal of the top layer in peroxide/ammonia mixture.

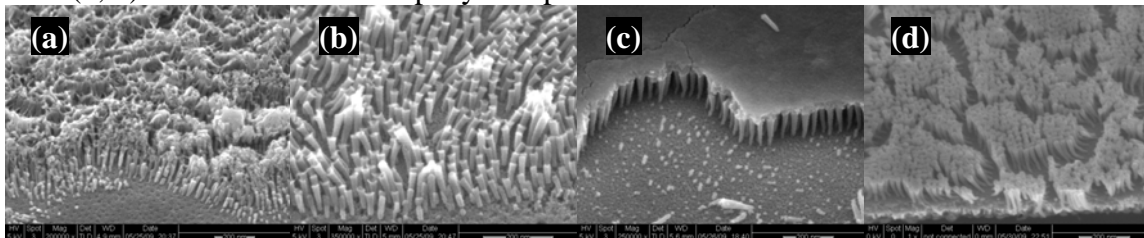


Figure 12: 45° SEM cross-sectional pictures of titania nanopillars deposited in 300 nm NFC templates on 100 nm titania underlayer precoated platinum substrate, with electrical sol-gel potential of 1.147V and durations of 30sec (a, b) and 2min (c, d), without treatment in mixture of 30% H₂O₂ and 29% NH₄OH (v:v=1:1) (a, c), or after 40sec dip (b) or after 160sec dip (d) in the mixture of H₂O₂ and NH₄OH.

As we learned from our cyclic voltammetry study, stir-bar agitation can remove the loose layer from the top of the deposited titanyl hydroxide gel. We considered this phenomenon could be used for selective removal of top layer, since the gel deposited in the pores of the template is protected and only the gel on top of the template can be swept by the flowing solution (as illustrated by *Figure 13(a)*). The titania nanopillars grown in 200 nm PMGI template by 3 min electrical sol-gel deposition with the solution stirred by a rotating stir-bar with a speed of ~300 rpm, is shown in *Figure 13(b)*. As expected, the less compact gel on top of the template and outside of the template pores are continuously swept away, while the gel inside the template pores is protected by the template and becoming more and more compact over time.

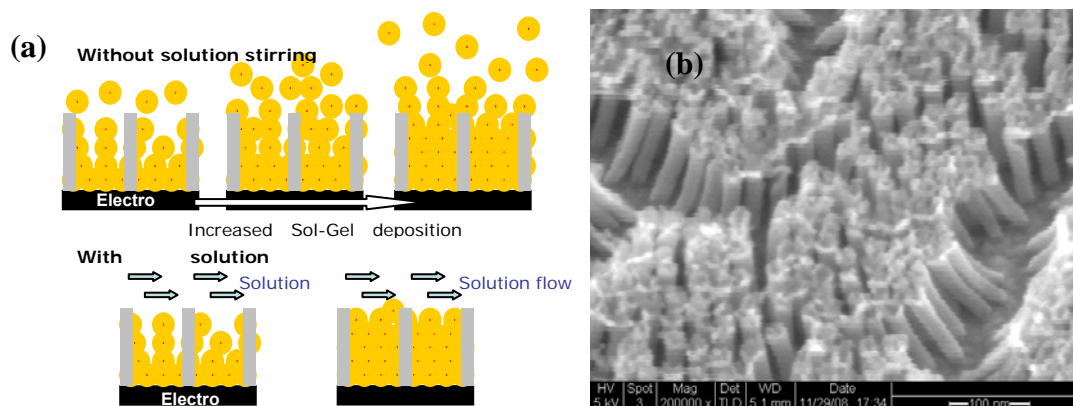


Figure 13: (a) The mechanism of electrically induced sol-gel deposition of titanyl hydroxide gel with a template, with or without stir-bar agitation of the solution during the sol-gel process, and with working electrode potential of -1.147V (referred to Ag/AgCl); (b) 45° SEM cross-sectional pictures of titania nanopillars sol-gel deposited in 200 nm thick polymer templates, with the working electrode potential of -1.147V (versus Ag/AgCl reference) for 3min under the stir-bar agitation speed ~300rpm.

2. Dye-Sensitized Solar Cells Fabricated on Fluorine Doped Tin-Oxide Substrates

In the last annual report, we showed I-V characteristics of dye-sensitized solar cells fabricated on platinum coated silicon wafers. The efficiencies of these cells were limited by the back-side illumination setup, because the silicon wafer was not transparent and the light had to be shined from the back-side, which means there was incident light energy

loss caused by absorption of the I/I_3^- electrolyte. Another factor that lowered the cell efficiencies was the Schottky junction formed by TiO_2 and the platinum substrate due to the large difference between their workfunctions. We fabricated dye-sensitized solar cells on fluorine doped tin-oxide substrates (FTO) [26]. The efficiency was increased to 0.45%, because the similar workfunctions between TiO_2 and FTO reduced the Schottky function effect and front-side illumination could be used which reduced energy loss caused by absorption of the electrolyte.

3. High-Aspect Ratio Polymer Template Etching with Gold Hardmask

For the block copolymer containing hybrid etch mask, even though the organosilicate domains has much lower etching rate for oxygen plasma, the integrity of the organosilicate mask will lost due to an increased lateral tension across it during etching. The lateral tension in the mask is caused by the non-uniform sizes of the spherical domains and the resulted non-uniform pores in the polymer to be etched. Deeply and densely packed pores are associated with lateral tension in the polymer, which shrinks those originally smaller pores while enlarging those originally larger pores to minimize the surface energy. As a result, lateral tension is generated in the net shaped organosilicate domain, which breaks this originally continuous domain and further worsens the non-uniformity of the pores sizes in the polymer layer to the degree of a totally lost pattern. In addition, since both the etching mask material (organosilicate) and the transfer layer material (NFC) are insulators, electrostatic charging might have played a role in the etching process by diverting the ions from the ideally vertical paths.

To resolve these problems, a harder and preferably conducting material, e.g. a metal, is desirable to replace the organosilicate as the mask during the prolonged polymer etching. Due to its chemical inertness and large atomic mass in contrast to the organosilicate, we chose gold as the hardmask material. The pattern in gold was created by argon sputter etching with the block copolymer hybrid as the mask layer. Then oxygen plasma etching recipes, similar to the ones for samples without the hardmask, were used to etch the polymer with the net-shaped gold layer as the hardmask. A lower pressure, 3 mT, was used during the first part of the etching to minimize undercut, and the normal pressure, 6 mT, was used thereafter to maintain the etching rate when the aspect ratio became large. As shown in (Figure 14(a, b)), about 500 nm thick, highly vertical pores were achieved with diameter of 20 nm and interpore distance of about 40 nm. Figure 14(c, d) show approximately 400 nm long titania pillars grown in the pores by 4 min of electrochemical growth with working potential of 1.147 V (referred to Ag/AgCl). The images show that nanopillars are in good contact with the substrate and almost all of the pores are filled with the nanopillars. To be noted is that the platen RF power of 24 W (Figure 14(b)) showed more uniform etching than 19 W (Figure 14(a)), which used to be optimal in the case without the hardmask, indicating that with the hardmask sputter etching component can be tuned up against chemical etching.

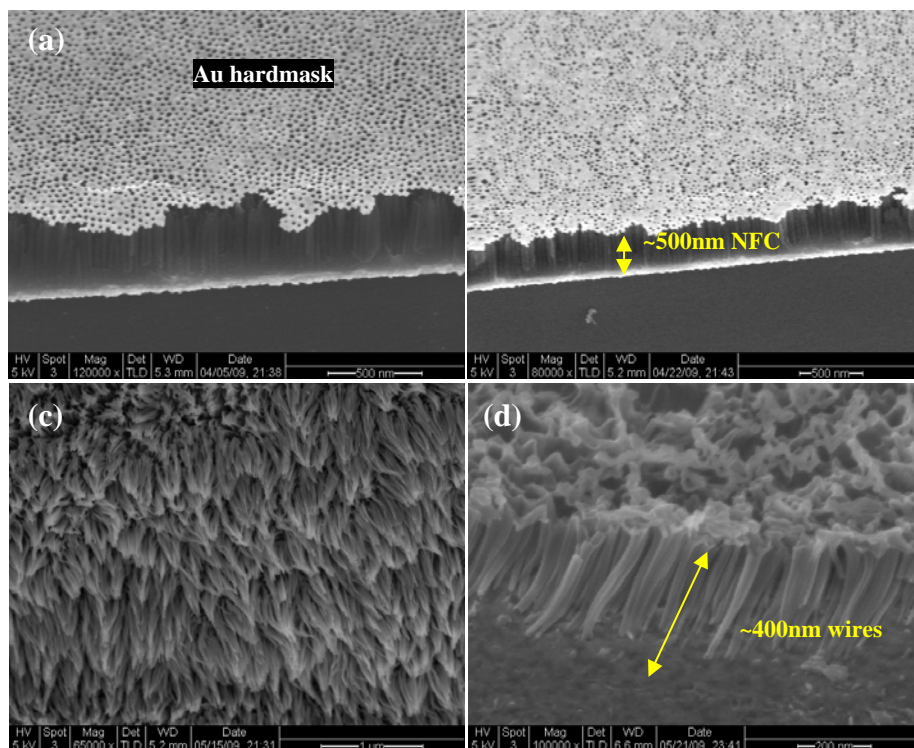


Figure 14: 45° SEM cross-sectional pictures: (a) 500 nm NFC layer etched in ECR etcher with O₂ 100sccm, ECR power of 50W, RF platen power of 19W, 3mT for 250sec and 6mT for 500sec (120sec cooling cycles were used after every 120sec of etching); (b) is the same as (a) except the RF platen power was 24W, the 3mT period was 600sec and the 6mT period was 360sec (100sec cooling cycles after every 100sec of etching); (c) Bottom view from a lifted portion and (d) cross-section view of titania nanopillars, sol-gel deposited for 4min with working electrode potential of -1.147V (referred to Ag/AgCl).

4. TiO₂ Nanopillar Multilayer Stacking

Another part of this project is to develop a novel type of multilayer titanium dioxide (TiO₂) nanopillar structure which can obtain better mechanical stability and larger surface area than single layer nanowire arrays. Lower effective surface area of the nanowires is due to two facts: First, longer nanowires are unable to stand straight by themselves without any supports; Second, nanowire arrays that are too dense tend to cluster which reduces the dyeable surface. We introduced a cover layer of TiO₂ on top of each layer of TiO₂ nanopillar array, which avoids nanopillar clustering or bundling and at the same time provides electrical connection between nanopillars in different layers. As a result, the nanopillar alignment is not required when layer by layer stacking is used to increase the total internal surface area of the TiO₂ nano-structure (as shown in Figure 15(a)).

We investigated different approaches to stack layer of nanopillar arrays to create a single-crystalline-like ordered TiO₂ nano-structure. Layer stacking of nanopillar arrays have been achieved by rolling of titanyl (TiO(OH)₂) gel filled polymer template prior to high temperature annealing, as illustrated in Figure 15(b) and (d). And more reproducible multi-layer stacking technique which involves TiO₂ nanopillar layer liftoff followed by layer transfer has been explored (as shown in Figure 15(c)) and preliminary results of

double layer stacking with this layer transfer technique have been obtained (as shown in Figure 15(e)).

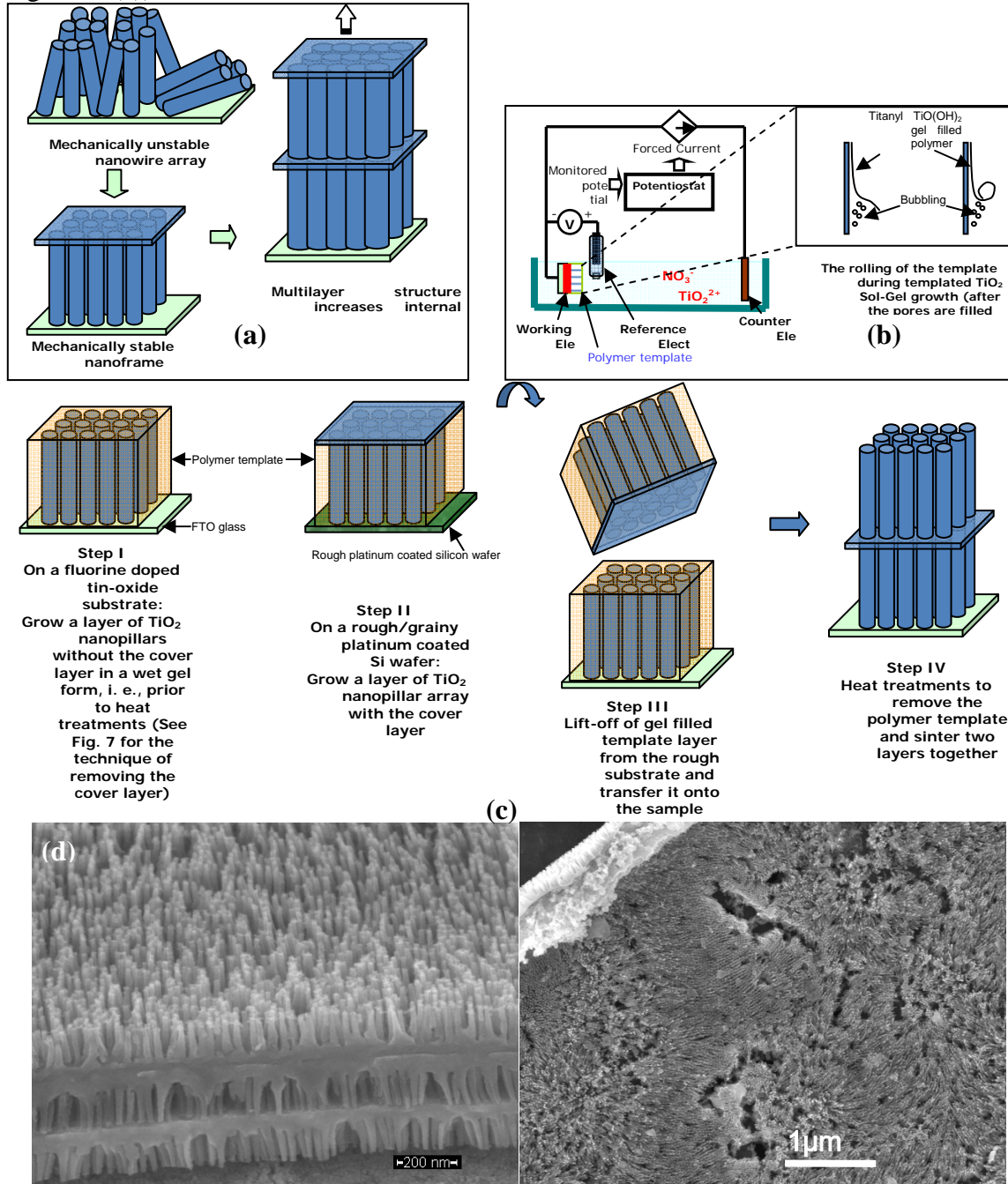


Figure 15: (a) The advantages of multilayer nanopillar structure: (1) Improved mechanical stability as compared to unsupported nanopillar array; (2) The newly introduced cover layer of TiO_2 on top of each layer of nanopillar array provide electrical connection between adjacent nanopillar layers. As a result, the nanopillar alignment is not required when layer by layer stacking is used to increase the total internal surface area of the TiO_2 nano-structure; (b) Multilayer TiO_2 nanopillar array fabricated by rolling titanyl ($\text{TiO}(\text{OH})_2$) gel filled polymer template prior to high temperature; (c) Process flow for TiO_2 nanopillar array layer transfer; (d) 45° SEM picture of multi-layer TiO_2 nanopillar arrays created by layer rolling; (e) Preliminary double layer result of 200nm TiO_2 nanopillar structure. (Upper layer lifted off by ultrasonic assisted electrical bubbling in 0.1M KNO_3 solution).

Progress

1. Array of Ag strips on a thin (50 nm) Si film cell was investigated by FDFD simulation and enhancements in photocurrent of over 43% could be obtained. Even higher enhancements (> 50%) could be reached for thicker cells (100nm-10 μ m) for which more waveguide modes can contribute to the overall enhancement.
2. FDTD simulation shows the nanoring antenna has the ability to tune the strong dipolar bonding resonance and hence the absorption enhancement peak very near the wavelength regions of the solar spectrum. In the case of the AIAs nanowire, there is a 6x enhancement at resonance near where the LSP mode of the individual ring occurs. The GaAs nanowire shows a much stronger enhancement of about 380x at around where the ring's symmetric bonding mode occurs.
3. A low cost and simple method was developed to fabricate the nanoring antenna and facilitate single nanowire growth in the center of the nanoring.
4. GaP nanowires solar hydrogen generation was demonstrated through monolithic photoelectrochemical process.
5. The MOCVD has been set up at Stanford for III-V high performance solar cell study equipped with special nitrogen doping feature.
6. Anatase TiO₂ nanoframe was grown directly on conductive and transparent substrates using templated Sol-Gel deposition to make nanowire structure more robust, which can greatly increase the mechanical stability of nanowire array solar cell. Multi-layer nanoframe stacking was demonstrated to extend the thickness of TiO₂ nanostructure.

Future Plans

1. Extend the FDFD simulation to 3-dimensional arrays and aperiodic structures that exhibit even higher efficiencies.
2. 3D simulation on the enhancement of the fabricated nanoring antenna structure.
3. Fabricate PV device using the nanoring and nanowires and test the performance.
4. Using III-V-N MOCVD grow nanowires for nanoring antenna and PEC applications.
5. Fabricate multilayer TiO₂ solar cells.

Publications

1. Ragip A. Pala, Justin White, Edward Barnard, John Liu, and Mark L. Brongersma, *Adv. Mater.* 21, 3504-3509 (2009).
2. E. S. Barnard, J. S. White, A. Chandran, M. L. Brongersma, *Optics Express* 16, 16529 (2008).
3. Chen, Y., S.-M. Park, H.-C. Kim, J. McVittie, C. Ting, and Y. Nishi, "High Aspect Ratio Titanium Dioxide Nanopillar Arrays from Templated Electrochemical Deposition", *Nanotechnology* 21, 185303 (2010).
4. Chen, Y., S.-M. Park, H.-C. Kim, J. McVittie, C. Ting, and Y. Nishi, "Direct Growth of High Aspect Ratio Titania Nanowires on Transparent Conductive Oxide Surface Using a Polymeric Nanotemplate", *MRS Fall Meeting*, Boston, MA, (Dec. 2009).

5. Chen, Y., H.-C. Kim, J. McVittie, and Y. Nishi, "Single-crystalline Like Multilayer Titania Nanopillar Arrays Synthesized by Templated Sol-Gel Deposition Followed by Layer Transfers", *MRS Spring Meeting*, San Francisco, CA (Apr. 2010).
6. X.-Y. Bao, B. A. Pinaud, J. Parker, S. Aloni, T. F. Jaramillo, H.-S. P. Wong, "Monolithic III-V Nanowire PV for Photoelectrochemical Hydrogen Generation", *35th IEEE Photovoltaic Specialist Conference*, Hawaii (June 2010).

Contacts

PIs:

H.-S. Philip Wong:	hspwong@stanford.edu
Peter Peumans:	ppeumans@stanford.edu
Mark L. Brongersma:	markb29@stanford.edu
Yoshio Nishi:	nishi@ee.stanford.edu

Graduate researchers:

Ying Chen:	mihuhou@stanford.edu
Jason Parker:	jaypark@stanford.edu
Trudie Wang:	trudie@stanford.edu

Post-doctoral researchers:

Xinyu Bao:	xinyubao@stanford.edu
Aaron Hryciw:	ahryciw@stanford.edu

Research Associates:

Jim McVittie:	mcvittie@cis.stanford.edu
---------------	--

References

1. R. A. Pala, J. White, E. Barnard, J. Liu, and M. L. Brongersma, *Design of Plasmonic Thin-Film Solar Cells with Broadband Absorption Enhancements*. *Advanced Materials*. **21**, 3504-3509 (2009).
2. E. S. Barnard, J. S. White, A. Chandran, and M. L. Brongersma, *Spectral properties of plasmonic resonator antennas*. *Opt. Express*. **16**, 16529-16537 (2008).
3. G. Veronis and S. H. Fan, *Overview of Simulation Techniques for Plasmonic Devices*, in *Surface Plasmon Nanophotonics*, M.L. Brongersma and P.G. Kik, Editors. 2007, Springer Berlin / Heidelberg, p. 169.
4. P. Nordlander, *The Ring: A Leitmotif in Plasmonics*. *Acs Nano*. **3**, 488-492 (2009).
5. J. Aizpurua, P. Hanarp, D. S. Sutherland, M. Kall, G. W. Bryant, and F. J. G. de Abajo, *Optical properties of gold nanorings*. *Physical Review Letters*. **90**, (2003).
6. E. M. Larsson, F. Hao, L. Eurenus, E. Olsson, P. Nordlander, and D. S. Sutherland, *Plasmon Hybridization in Stacked Double Gold Nanorings with Reduced Symmetry*. *Small*. **4**, 1630-1634 (2008).
7. S. Wang, D. F. P. Pile, C. Sun, and X. Zhang, *Nanopin plasmonic resonator array and its optical properties*. *Nano Letters*. **7**, 1076-1080 (2007).
8. F. Hao, P. Nordlander, M. T. Burnett, and S. A. Maier, *Enhanced tunability and linewidth sharpening of plasmon resonances in hybridized metallic ring/disk nanocavities*. *Physical Review B*. **76**, (2007).
9. F. Hao, Y. Sonnefraud, P. Van Dorpe, S. A. Maier, N. J. Halas, and P. Nordlander, *Symmetry Breaking in Plasmonic Nanocavities: Subradiant LSPR Sensing and a Tunable Fano Resonance*. *Nano Letters*. **8**, 3983-3988 (2008).
10. H. Wang, Y. P. Wu, B. Lassiter, C. L. Nehl, J. H. Hafner, P. Nordlander, and N. J. Halas, *Symmetry breaking in individual plasmonic nanoparticles*. *Proceedings of the National Academy of Sciences of the United States of America*. **103**, 10856-10860 (2006).
11. E. Prodan and P. Nordlander, *Plasmon hybridization in spherical nanoparticles*. *Journal of Chemical Physics*. **120**, 5444-5454 (2004).
12. T. H. Park, N. Mirin, J. B. Lassiter, C. L. Nehl, N. J. Halas, and P. Nordlander, *Optical properties of a nanosized hole in a thin metallic film*. *Acs Nano*. **2**, 25-32 (2008).
13. J. Ye, P. Van Dorpe, L. Lagae, G. Maes, and G. Borghs, *Observation of plasmonic dipolar anti-bonding mode in silver nanoring structures*. *Nanotechnology*. **20**, (2009).
14. F. J. Beck, A. Polman, and K. R. Catchpole, *Tunable light trapping for solar cells using localized surface plasmons*. *Journal of Applied Physics*. **105**, (2009).
15. K. Munehika, J. M. Smith, Y. Chen, and D. S. Ginger, *Plasmon line widths of single silver nanoprisms as a function of particle size and plasmon peak position*. *Journal of Physical Chemistry C*. **111**, 18906-18911 (2007).
16. J. Ye, L. Lagae, G. Maes, G. Borghs, and P. Van Dorpe, *Symmetry breaking induced optical properties of gold open shell nanostructures*. *Optics Express*. **17**, 23765-23771 (2009).
17. J. Aizpurua, L. Blanco, P. Hanarp, D. S. Sutherland, M. Kall, G. W. Bryant, and F. J. G. de Abajo, *Light scattering in gold nanorings*. *Journal of Quantitative Spectroscopy & Radiative Transfer*. **89**, 11-16 (2004).
18. F. Hao, E. M. Larsson, T. A. Ali, D. S. Sutherland, and P. Nordlander, *Shedding light on dark plasmons in gold nanorings*. *Chemical Physics Letters*. **458**, 262-266 (2008).
19. K. Li, L. Clime, L. Tay, B. Cui, M. Geissler, and T. Veres, *Multiple surface plasmon resonances and near-infrared field enhancement of gold nanowells*. *Analytical Chemistry*. **80**, 4945-4950 (2008).
20. E. M. Larsson, J. Alegret, M. Kall, and D. S. Sutherland, *Sensing characteristics of NIR localized surface plasmon resonances in gold nanorings for application as ultrasensitive biosensors*. *Nano Letters*. **7**, 1256-1263 (2007).
21. C. X. Lin and M. L. Povinelli, *Optical absorption enhancement in silicon nanowire arrays with a large lattice constant for photovoltaic applications*. *Optics Express*. **17**, 19371-19381 (2009).
22. B. M. Kayes, H. A. Atwater, and N. S. Lewis, *Comparison of the device physics principles of planar and radial p-n junction nanorod solar cells*. *Journal of Applied Physics*. **97**, 114302-11 (2005).
23. T. Bak, J. Nowotny, M. Rekas, and C. C. Sorrell, *Photo-electrochemical hydrogen generation from water using solar energy. Materials-related aspects*. *International Journal of Hydrogen Energy*. **27**, 991-1022 (2002).
24. Z. Miao, D. Xu, J. Ouyang, G. Guo, X. Zhao, and Y. Tang, *Electrochemically Induced Sol-gel Preparation of Single-Crystalline TiO₂ Nanowires*. *Nano Letters*. **2**, 717-720 (2002).

25. C. Natarajan and G. Nogami, *Cathodic Electrodeposition of Nanocrystalline Titanium Dioxide Thin Films*. Journal of the Electrochemical Society. **143**, 1547-1550 (1996).
26. C. Ying and et al., *Synthesis of TiO₂ nanoframe and the prototype of a nanoframe solar cell*. Nanotechnology. **21**, 185303 (2010).